AR-319-VOL-2

Real Gas / Blunt Cone Phase II Report

George S. Deiwert

Georg Eitelberg

1. INTRODUCTION

In this chapter recent activity in real-gas database definition and code validation will be summarized. In the Phase I report of the Working Group (WG) 18[1], aerothermodynamic problems were classified, for purpose of discussion, into seven types: aerodynamic parameters, viscous/shock interaction, boundary-layer transition, forebody-heating/heat-transfer, radiation and ablation, lee and base-region flow, and low-density flow. Several of these problem types were the subject of various chapters of the Phase 1 report describing real-gas effects and ground test facility issues.

In this chapter some background and objectives outlined in the real-Gas effects Chapter V of the Phase 1 report will be reviewed. The results of the blunt cone test campaign developed under the auspices of the WG18 activity to study real-gas phenomena will be summarized, including the experimental and computational programs, issues and questions, and recommendations. Further, recent progress in other real-gas areas beyond the blunt cone test campaign will be discussed. Finally, a summary in which the present status of our understanding of real-gas issues will be presented.

2. BACKGROUND/OBJECTIVES

Real-gas effects are important in hypersonic flows both in terms of their influence on aerodynamic performance and their effect on aerothermodynamic heating. It is recognized that high-enthalpy, ground-based test facilities cannot fully simulate flight conditions and that they exhibit unique real-gas behavior themselves. Hence, the process for developing validated analysis tools is one in which real-gas CFD is involved in all aspects of a real-gas ground-test program. CFD is used to design and define the experiment, to define the ground-facility test conditions, and to simulate the ground-test experiment itself. The ground-test data, in turn, are used to validate, or calibrate, the CFD simulations. Only in this manner can sufficient confidence be gained and real-gas analysis tools be validated.

In the Phase I report[1] the issues of real-gas effects on aerodynamic coefficients, forebody heating/heat transfer, and lee and base flows were discussed in the chapter on real-gas effects, chapter V. Viscous interactions were discussed in Chapter II, transition to turbulence in Chapter III and low density in Chapter IV. Radiation and ablation were not specifically treated.

Ground-facilities required to provide meaningful data for the real-gas issues were discussed in Chapter V, in VI regarding calibration requirements, and in Chapter VIII regarding future needs.

The development of validated analysis tools for hypersonic flows was described and involves a process in which real-gas CFD development and application and experimental testing are performed hand-in-hand, synergistically, until the validation is complete. Hypersonic flows inherently involve real-gas phenomena. The validation of CFD tools requires considerations asso-

ciated with perfect-gas CFD validation *plus* consideration of additional complexities associated with real-gas phenomena. These real-gas complexities include thermal and chemical time scales, multiple gas species, internal-energy flow variables and properties, and coupled fluid/chemical processes.

An effort was made to identify existing real-gas databases for the subject hypersonic flow problems. These included published studies involving the flow field about building block configurations including hemispheres, cylinders, and blunt cones as simulated in ground-based test facilities, and flight data obtained on the spherically blunted cone in the RAMC flight test program.

Additional building block experiments involving bluff and slender cones were identified, and new studies were recommended to augment the existing database for both compressive and expanding flows.

In this regard a blunt-body base-flow test configuration was developed as part of the WG18 activity. The results of this activity are the subject of the next section of this report.

Configuration studies on the shuttle orbiter configuration and the orbiter-like configuration Halis were also considered in the WG18 activity and were described in some detail in Ref. 1 and Chapter V of the present report.

In the following section, a detailed report of the blunt cone test campaign will be presented.

3. BLUNT CONE TEST CAMPAIGN

The blunt-body/wake closure problem was selected to help identify real-gas effects, including thermal non-equilibrium and rarefaction. Experimental and computational investigations have been made for low-density conditions reproducible in rarefied gas wind tunnel experiments[2-7] and high-enthalpy conditions reproducible in impulse shock tunnel facilities[8-10]. Several participants committed to perform tests on simple configurations, the most often-used one being the 70-degree half-angle blunt cone, either sting-mounted or free-flying (see Fig. 1). This geometry is the same forebody as used in the NASA Viking missions, and the geometry for the Mars Pathfinder probe.

Initially, a series of overlapping tests was proposed for three experimental facilities: the 16-inch shock tunnel at the NASA Ames Research center, Moffett Field, CA, the HEG piston-driven shock tunnel at the DLR-Göttingen, Germany, and the Large Energy National Shock Tunnel (LENS) at CALSPAN, Buffalo, NY. All three facilities were to examine a flow expanded through a nozzle of area ratio approximately 1600:1 to provide essentially equivalent free-stream conditions. The common test condition is based on the driver stagnation enthalpy and pressure conditions for this flow expansion, namely 10 MJ/kg, and 500 bar.

Each facility was to be operated at the same enthalpy and the same Mach and Reynolds number (H_0 = 10 MJ/kg, M = 7, and $\bullet_0$ = 500 bar). In addition, tests in the Ames facility were planned at total enthalpies of 5 and 14 MJ/kg at total pressures of 100 bar, in the DLR HEG facility at enthalpies of 20 MJ/kg and total pressures of 500 and 1000 bar, and in the LENS at enthalpy 5 MJ/kg and pressures of 500 and 2000 bar.

The lower enthalpy levels produce only modest levels of dissociated oxygen and no dissociated nitrogen. At 10 MJ/kg there will be substantial oxygen dissociation and negligible nitrogen dissociation. At 20 MJ/kg there will be substantial dissociation of both oxygen and nitrogen. Nitrous

oxide (NO) will be produced under all test conditions.

The main motivation for these tests was to provide data for numerical code validation, but the tests were also designed to give further information on facility behavior and quantification[1]. The code validation portion of the tests was designed to quantify the shear layer separation point, its turning angle and wake closure in the presence of flows exhibiting real-gas effects. The unsteady character of the near wake would also be documented, if possible. Body surface instruments would provide calibration/validation data for computational fluid dynamic (CFD) simulations. Both sting-mounted and free-flight models would be necessary to assess and quantify the influence of the sting in the instrumented model. Issues in the facility behavior context included shock standoff distance and shape, information about which can help characterize dissociation effects behind the bow shock. Also of facility behavior interest is the extent of the expansion wave over the shoulder of the blunt body. This data would help obtain global information about the properties of the free stream.

Several different experiments and computations have been completed for a variety of conditions[2-10]. Here, we concentrate on the hypersonic, high enthalpy conditions where real-gas effects must be considered. Experimental data for the high enthalpy flow conditions for this series have been reported by Kastell et al.[9] from HEG, and by Holden et al.[10] from LENS. The tests planned for the 10-inch shock tunnel at NASA Ames have not yet been performed.

Described herein are numerical simulations of the flow fields from the HEG and LENS high enthalpy experiments at the common test condition of 10 MJ/kg and 500 bar using both NS and DSMC solvers. The results from each code are compared not only to the experimental data, but to each other as well. Thermal non-equilibrium is examined using both codes, and representations of rarefaction effects are studied using the DSMC results. The ability of CFD to accurately simulate these high enthalpy flows is evaluated in terms of both computational accuracy and comparison to experimental data.

1.1. Computational Methods

The NEQ2D[11] code (also referred to in the literature as NASCAND or GIANTS) is used for all continuum flow-field computations in this paper. It uses the two-dimensional axisymmetric Navier-Stokes equations and expands them to allow for the presence of multiple species and Park's two-temperature model[13] (translational/rotational and vibrational/electronic temperatures). The equations are solved by a fully implicit, flux-split, Gauss-Seidel relaxation numerical technique. A five species air model is used (N2, O2, N, O, NO) in the solutions. The computational mesh (see Fig. 2a) is generated by the HYPGEN code[14] and is constructed so that all grid lines intersect the model body orthogonally. Exponential stretching is used where grid spacing changes are required normal to the model surface. Changes in step size along the surface of the model are smoothed to assure a clean computational grid. Zero wall velocity and room temperature boundary conditions are used in the computations. Since the wall temperatures are low, non-catalytic boundary layers are assumed.

The DSMC code is used an axisymmetric particle solver by Gallis and Harvey[4], which uses the Variable Soft Sphere (VSS) model from Koura and Matsumoto[15]. The code uses a multi-regional mesh (see Fig. 2b) to achieve the best possible distribution of cells in the computational

domain. Weighting factors are used in the radial direction to reduce the number of particles required in the simulation. The code simulates translational, rotational, vibrational, and electronic energy modes. The vibrational and the electronic modes are treated in quantum states. All other properties are treated as continuous distributions. A modification of the Maximum Entropy method of Levine and Bernstein[16] is used for the simulation of chemical reactions and energy exchange. The wall boundary conditions are fully accommodating, diffusely reflective, and noncatalytic.

The DSMC code described by Gallis and Harvey[4] is not modified for use in this work, but it uses results from NS forebody computations as its startline condition for computing the wake flow, However, the NS code, NEQ2D, is adapted for this work from previous versions of the code. First, the original FORTRAN code is converted to run as a C code for this study. Second, the original NEQ2D code uses both a second order differencing scheme and a first order upwind differencing scheme. The upwind differencing is intended only for use in near and through shock waves (it is unstable otherwise). The trigger for deciding which of the two differencing schemes is used monitors when the pressure gradient exceeds a critical value. The original gradient algorithm is only one-dimensional in the streamwise direction. The code is revised to use a two-dimensional gradient in both the streamwise and orthogonal directions. This removes some mesh-sensitivities in the stagnation point region, which were seen with the original code formulation. Finally, the code is changed to use thermal and vibrational energy as boundary conditions rather than temperature. This technique enhances low temperature (near 300 K) solution stability near the walls.

1.2. Shock Tunnel Facilities

The three shock tunnel facilities, which have been used to perform experiments with blunt cone models, are the 42-inch combustion-driven shock tunnel, located at the NASA Ames Research Center, the high-enthalpy free piston-driven shock tunnel (HEG) at DLR-Göttingen, and the Large Energy National Shock Tunnel (LENS) at CALSPAN. Though the facilities have differing operating characteristics, all three shock tunnels are or were capable of simulating high-pressure, and/or high-enthalpy conditions required to study hypersonic flows with real-gas effects.

A schematic of a generic shock tunnel facility is shown in Fig. 4. The NASA Ames facility has been decommissioned and is not available for further testing. It was 30.0 m in total length and consisted of a 7.66 m driver tube (diameter of 68.6 cm), a 12.2 m shock tube (diameter of 15.8 cm), and a 2.74 m, 10 degree half-angle conical supersonic nozzle segment at the end of the driven tube. The nozzle exit diameter was 1.1 meters. An open jet test section was located at the end of the nozzle. In this shock tunnel, the driver section of the shock tunnel was filled with a light combustible mixture, and the driven section (shock tube) was filled with the test gas. When the main diaphragm ruptured after ignition of the driver gas, a shock propagated towards the end of the driven tube. A secondary diaphragm located at the nozzle entrance was used to accurately control the driven tube fill pressure. The reflected shock burst the secondary diaphragm and initiated the nozzle flow. The test time for this facility was designated as the length of time (for the experimental conditions used in this paper, on the order of several milliseconds) during which quasi-steady nozzle stagnation conditions were achieved before the driver gas

arrived at the test section[17]. The test models in this facility (and in the other two shock tunnels as well) were situated in the test chamber at the nozzle exit.

The HEG facility produces flows similar to the NASA 42-inch shock tunnel. The driver compression is supplied by a moving piston, rather than from combustion, and its scale is larger. It is 60.0 m in total length, with a 33.0 m driver tube (diameter of 55.0 cm), a 17.0 m shock tube (diameter of 15.0 cm), and a 3.75 m supersonic contoured nozzle. The diameter at the nozzle exit is 0.88 meters. Test times are several milliseconds long for high enthalpy operating conditions[18].

The LENS facility is similar in size to the HEG facility, but the operation differs slightly. The driver tube is pressurized and can be heated prior to the diaphragm rupture, rather than using a combustion or free-piston driver. A double-diaphragm configuration vents pressure in an intermediate chamber to fire the tunnel. The facility is 44.0 m in total length, with a 7.9 m driver tube (diameter of 29.2 cm), a 17.5 m shock tube (diameter of 20.3 cm), and a 6.2 m nozzle. The nozzle exit diameter is 1.22 m. The test times are also several milliseconds long under high enthalpy operating conditions[19].

1.3. Shock Tunnel Flows and Numerical Simulations

The reservoir conditions driving the nozzle expansion are the flow properties behind the reflected shock at the end of the driven tube (shock tube). Those stagnation conditions are usually calculated from the measured initial pressure in the driven tube and the measured incident shock speed. The most commonly used computer code for estimating shock tunnel reservoir conditions is called ESTC[20]. For a "tailored" shock tunnel operating condition, the gas left behind the reflected shock near the driven tube end wall has a zero flow velocity. The gas is assumed to be in chemical equilibrium since the pressure and temperature a re high, and the flow is nearly stagnant.

The flow in the facility nozzle is calculated using quasi-1D and/or 2D/axisymmetric formulations capable of capturing the non-equilibrium effects. Several numerical methods and computational tools have been used to solve the Navier-Stokes equations for this application. In order of increasing complexity as well as accuracy, some of the recently used codes implemented for these applications are NENZF[21], LSENS[22], STUBE[23] (all three of these codes assume inviscid flow and quasi-1D equilibrium chemistry from the reservoir to the nozzle throat and thermal/chemical non-equilibrium from just downstream of the throat to the nozzle exit), a 3D Euler/NS solver by Hannemann[24,25], and GASP[26] (the last two being viscous, multidimensional Navier-Stoke codes with full thermochemical non-equilibrium). The multidimensional computations have been recently validated with shock tunnel experimental pitot pressure data by Hannemann[24,25] and Papadopoulos et al.[27].

The expanded driven gas enters the test section of the shock tunnel at the nozzle exit and washes over the model. After a quasi-steady flow is established (as determined by pressure and heat flux measurements during the run time of the facility), the actual usable test time begins. The test time is terminated when the driver gas reaches the test section and significantly changes the flow field around the model. Hence, the quoted free-stream conditions in the test section of the facility are determined by a combination of experimental and computational methods. The free-stream conditions for the experi-

mental data examined in this paper are summarized in Table 1. These values are used as the input to the NS code used in this study.

Table 1: HEG, LENS and NASA 42-inch test conditions[8,9,12]

	HEG Run 132	HEG Run 133	LENS Case E	NASA 42-inch
P_0 (Mpa)		55	49.11	28.98
H_0 (MJ/kg)	11.48	11.97	11.03	9.3
T_0 (K)	6712.9	6564.9	6483.3	-
M_∞	10.12	9.99	8.53	14.9
V_∞ (m/s)	4539.5	4470.7	4430.3	4150
T_∞ (K)	489.9	488.1	673.1	190
P_∞	588.4	575.5	692.1	18.24
ρ_∞ (kg/m^3)	0.00409	0.00402	0.0035	0.00031
Molecular wt.	28.3	28.32	28.4	28.86
N_2 (mol.cond.)	0.7279	0.7289	0.7363	0.785
O_2 (mol.cond.)	0.1475	0.1493	0.157	0.215
N (mol.cond.)	4.80E-07	4.50e-07	0.0091	1.00E-08
O (mol.cond.)	0.0478	0.0446	0.0387	1.00E-08
NO (mol.cond.)	0.067	0.0675	0.0589	1.00E-08

The subscripts 0 and ∞ refer to reservoir stagnation and free-stream conditions, respectively. Conditions as determined by experimental calibration data, by the shock tube code ESTC[20] for air, and by STUBE[23] for HEG[8,29], GASP[26], for LENS[9] and Refs. 17 and 28 for the 42-inch tunnel.

1.4. Results

The blunt cone geometry has been the object of both experimental and computational scrutiny for several years[2-9]. Much of the work has been concentrated on the lower density cases, in which the NS codes break down and would not be expected to yield accurate results. DSMC codes have been used for many of those investigations, and that work has yielded good comparisons between computations and experiments. At the higher enthalpy flow conditions in this investigation, the densities are expected to be at levels where NS codes stand a better chance of producing reasonable accuracy. At the same time, the DSMA codes will have difficulty dealing with the higher densities and the large density gradients seen over the computational domain.

1.5. Navier-Stokes Forebody solutions

The NEQ2D code has been used previously in computations for a 70-degree blunt cone model forebody by Stewart and Chen[12]. In that work, the geometry in the shoulder region of the body differed slightly from the AGARD WG18 test model. A separate grid (not pictured) is generated to run this case for code validation purposes since changes have been made to the NEQ2D code for this study.

The computational and experimental results for the Stewart and Chen work can be seen in Fig. 4, where the heat flux is plotted along the body surface. There is a difference between those results and the runs with the updated version of NEQ2D. Some of these differences can be attributed to changes in the boundary conditions used in the newer version of the code, which eliminated some numerical problems when simulating room temperature walls[30]. Also, the older version of the code contained eigenvalue limiters, which were adjusted when comparing the CFD results to the experimental data[31]. The newer version of NEQ2D has had the limiters removed so the results cannot be "tuned" to fit to an experimental database. Additionally, the change in the algorithm for computing gradients in the stagnation region resulted in grid independent solutions for the forebody computations

in this paper. The previous version of the code produced mesh-dependent stagnation point fluxes and was the reason for implementing the previously discussed modifications to the NEQ2d code.

The match of the present NS results to the experimental data is similar to that reported by Stewart and Chen. The normalized heat fluxes match significantly better in this study, but the actual heat fluxes are underpredicted by 23% at the nose. The Chen CFD overpredicts the stagnation point heat flux data by only 6.5%, but eigenvalue limiters were used with the code, and the results remained somewhat mesh-sensitive in the nose region[31]. Stewart reported a 10% uncertainty in the data, which is indicated by the error bars in Fig. 4. However, issues of heat flux uncertainties in light of new data analysis methods for coaxial thermocouples are currently being investigated[9,32,33]. This work may eventually account for some of the differences in the absolute values of these heat flux data.

Forebody data are also available from Kastell et al.[9] and Holden et al[10]. HEG Run 132 results can be seen in Fig. 5, where the normalized computed and experimental heat fluxes are within approximately 15% of each other. The shape of the heat flux profile around the shoulder of the body is well simulated, but the shape of the forebody heat flux curve is somewhat different. Also, the magnitudes of the stagnation point heat fluxes differ by 37% (the stagnation point heat flux value of approximately 500 W/cm^2 was extrapolated from data presented by Legge[34]). Here the questions concerning the coaxial thermocouples were eliminated by using the same material for the model (chromel) as one of the thermocouple materials. It should be noted that absolute errors for the HEG experimental data have not yet been reported in the available literature, though they are expected to be in the 10% range[32]. Results for LENS Case E show an underprediction of the both normalized and actual heat fluxes compared to experimentals, but the data in the forebody are very limited. The LENS experimental stagnation heat flux value was extrapolated from the limited data to allow for comparative evaluations. The value used, 380 W/cm^2, was not available experimentally.

1.6. Navier-Stokes Wake Solutions

NS wake computations have been completed for HEG Runs 132, 133 and LENS Case E. The results can be seen in Figs. 6-9. Since all of these runs showed similar behavior, only one case, HEG Run 132, will be shown as representative of the three runs. Where significant differences appear, they will be noted individually.

Fig. 6 shows the density field (in kg/m^3) for HEG Run 132. The wake region is clearly defined by the locations of the shock and the free stream. The white area in front of the blunt body contains higher density gas flow than is indicated by the contour levels in the figure. This region was excluded from the contour plot to allow visualization of the bow shock and not to wash out all flow features in the wake. The results show the expected region of low density immediately behind the blunt body in the recirculation zone. The density begins to increase at the point where the shear layer impinges on the sting. A weak compression region can also be seen above the sting at about 1.5 nose radii from the corner where the sting mated with the blunt body. This weak compression contour appears at an angle of approximately 15 degrees to the sting.

Traces of the particle paths are shown in Fig. 7. The main recirculation zone is clearly defined, and a smaller zone is seen in the corner where

the sting joins with the blunt body. A final small recirculation zone is located just behind the point of separation along the back of the blunt body near the shoulder. A plot of Mach number contours in Fig. 8 identifies the two smaller recirculation zones as subsonic, but inside the main recirculation cell exist two separate regions where the Mach number exceeds one slightly (approximately Mach 1.5). These supersonic recirculation flows have also been seen by Anagnost [35] and Haas[36] in similar NS blunt body computations without a sting.

The wake can be examined for thermal non-equilibrium by looking at the normalized difference between vibrational and translational-rotational temperatures ($(T_{t\text{-}r}-T_v)/T_{t\text{-}r}$) in the two-temperature model. Fig. 9 shows that there exist regions near the backside of the body and along the sting where the vibrational temperature is still out of thermal equilibrium. This is due to the low densities in those regions, the speed of the flow, and the cooling of the gas due to heat transfer to the sting. There is an insufficient amount of time (i.e., number of molecular collisions in these regions) for the vibrational energies to equilibrate. The frozen, non-equilibrium expanding flow in the far wake, behind the blunt body and above the sting, is also clearly seen in Fig. 9.

Fig. 10 shows the heat flux on the sting for the NS results and the corresponding experimental data for HEB Run 132 and LENS Case E. For HEG Run 132, the location of the local heat flux maximum on the sting is similar for both the experimental data and NS computations (between S/R_n values of 7 and 8). However, the magnitudes of the normalized heat flux differ by a factor of 3.4, and the actual heat fluxes differ by a factor of 5.4. In contrast, the LENS Case E computations and experiments show excellent agreement in the magnitude of the local heat flux maximum on the sting, at approximately 6.5% of the stagnation point value (actual heat fluxes differ by approximately 26%). But, the experimental data indicate the maximum is farther down on the sting near an S/R_n of 10.5. Fig. 11 shows a combination of Figs. 5 and 10 on a single log plot. In this way, one can better see the global matching of the heat fluxes from computations and experiments. In some regions, the match appears reasonably visually, but due to the log nature of the plot, absolute errors are hard to read and the reader must refer to the original linear plots or numerical values.

One possible explanation for the disagreement in the LENS and HEG experiments is the existence of a turbulent shear layer in the HEG wake flow. As a quick investigation into this possibility, the computational viscosity was arbitrarily increased (as a crude model for turbulence) significantly in the wake region on a test run for the HEG Run 132 condition. The heat flux along the sting showed that a threefold increase before numerical instabilities near the rear corner where the sting mates with the blunt body forced the computation to stop. Though this is no definitive indicator of any answer to the differences in the experimental data, it certainly indicates that an investigation of the state of the shear layer could be a worthy avenue of pursuit both computationally and experimentally. Another recent study (Holden et al.[37]) also indicates that turbulence might be the cause for the differences in the experimental data between HEG Run 132 and LENS Case E. Studies are in progress to experimentally study the state of the shear layer in the wake behind this blunt body at NASA Langley Research Center in perfect gas nitrogen flows to help demonstrate the onset of turbulence in these wake flows[32].

Another possibility for the differences in experimental data is that the flow in either or both experimental facilities may not be fully established in the wake. Measurements for both pressure and heat flux in LENS indicate that the flow has been established[10], but Kastell et al.[9] and Horvath[32] have examined HEG heat flux data using the method of Holden et al.[10], as well as their own method, giving ambiguous results on the existence of an established flow. If the flow indeed is unsteady, this could be from a lack of test time for flow establishment or the result of an inherent unsteadiness in the flow field. This kind of unsteadiness has been demonstrated computationally by Anagnost[35] using a 3D unsteady code for flow over a 70 degree blunt cone without a sting.

1.7. DSMC Wake Solutions

Although the high densities in front of the body preclude the use of a particle code in that region, the rapid expansion of the flow around the shoulder of the body drops the density significantly so that DSMC codes can be used. Previous simulations of the LENS Cases B and C, using DSMC codes, have shown that the code was spending most of the time calculating the flow field in front of the body[2,4]. There, the density rises up to 90 times the free-stream density. To simulate these high-density regions, most of the particles are concentrated in the compression region, while the rarefied wake are is left with only a few particles, thereby deteriorating the statistics of the simulation in this region.

On the other hand, the ability of the NS solvers to provide physically correct solutions in rapidly expanding low-density flows, such as the one behind the shoulder of the body, has been questioned. Recent studies into the breakdown of the continuum assumption[37] may be accelerated due to numerical diffusion introduced by the continuum solver or due to non-equilibrium chemical relaxation phenomena. To address this problem and the problem of a more balanced distribution of the particles in this study, solutions have been sought that include the use of two different calculations for the wake and the forebody regions. The code to be used for the forebody is the aforementioned NEQ2D code[11]. The results of the NS solver for the forebody will be used to provide the input conditions for the DSMC code to calculate the flow in the wake. For the purposes of this study, the coupling of the two codes (NS to DSMC) was made along a straight line parallel to the vertical axis, starting from the shoulder of the body (where the normal to the surface is in the vertical direction). This coupling section has been used before by Moss et a.[2] for the same geometry. The DSMC code is started with the assumption of vacuum in the wake, while the input boundary is set to reproduce the conditions calculated by the NS code along the startline.

Two cases were calculated, the LENS Case E and HEG Run 132. The grid used for these calculations is shown in Figure 2b. It is multi-block structured grid with 18,000 cells, in which 300,000 particles were used. Experience has shown that the heat flux is a sensitive indicator of code convergence. When no significant changes in heat fluxes were seen in DSMC data samples, the solution was considered converged.

Fig. 12 presents the density profile (in kg/m^3) for this case. The flow comes from left to right. The shock wave expands over the shoulder of the body into the wake region. The rapid expansion around the shoulder causes the density and the temperature to drop in the wake. The diffuse recompression wave (also seen in the NS re-

sults) that starts from the shoulder causes a localized density rise along the sting where the density rises to 70% of the free-stream density (60% in LENS Case E). The impact of the recompression wave on the sting is followed by an increase of the heat transfer and pressure in the same area. The angle of the compression from the sting is similar to the NS code results (approximately 15 degrees).

Fig. 13 shows particle traces for HEG Run 132. A single vortex is seen in the wake region. The smaller recirculation zones are not visible due to the low densities in that region, coupled with a low number of particles in these cells. Finer grid resolution, as well as more particles, would result in better statistics in the se cells, and the more flow structure might be seen. The particle paths are seen to impact the body surface in the corner where the sting mates with the blunt body. This is also a direct consequence of the insufficient resolution of the DSMC computation in that region. The LENS Case E results show traces of a second vortex near the tip of the body. The grid resolution at the back of the body, though, did not allow a better representation of the flow.

Fig. 14 shows a Mach number contour for HEG Run 132 from the DSMC computations. Some similarities are seen in comparison to the NS results in Fig. 8, especially in the far field flow. Even with the lack of resolution in the corner, small pockets of supersonic flow are seen in the DSMC, as was also seen in the NS code results. Fig. 15 shows the normalized differences between the vibrational and translational-rotational temperatures ($(T_{t\text{-}r} - T_v)/T_{t\text{-}r}$) used in the DSMC work. This gives an indication of the non-equilibrium in the flow-field. Equilibrium (value of 0) is only met in the free-stream while most of the wake, and in particular, the recirculation area behind the body are in thermal non-equilibrium. It is worth noting that equilibrium is hardly achieved along the sting of the body in the boundary layer. This non-equilibrium flow must be attributed to the cooling of the gas that impacts on the room temperature sting. This result is very similar to the NS code results seen in Fig. 9. However, the majority of the flow-field shows differences between the NS and DSMC work for the normalized vibrational temperatures. The DSMC results for both cases show no differences in the translational and rotational temperatures, validating the use of the two-temperature model in the NS code.

Figs. 10 and 11 present DSMC and NS surface heat fluxes in the wake region for the HEG Run 132 and LENS Case E experiments. The peak heat fluxes for both DSMC results occur with almost identical locations (S/R_n values of approximately 10.5) and normalized magnitudes (18% of the stagnation point value). But these computed normalized values are distinctly different from either experimental data set, and the actual magnitudes of the two DSMC peak heat fluxes differ by 30%. Also, the DSMC normalized heat flux for the HEG Run 132 is 18% below the experimental data point, but for LENS Case E, the DSMC normalized heat flux is a factor of 2.8 higher than the data. Thus the DSMC and NS codes are only partially successful in matching the experimental measurements of heat flux on the body in the wake.

1.8. Flow Visualization

An experimental interferogram for HEG Run 133 (a very similar condition to Run 132) has also been reported[9]. The NS output for the HEG Run 133 condition was used to generate a computational interferogram using the CISS (Constructing Interferograms, Schlieren, and Shadows-

graphs) code[38]. The experimental and computed interferograms can be seen in Fig. 16. The top portion of the figure is the experimental data, and the bottom portion is the mirror image of the computed result. The agreement is excellent, and fringe-shift measurements show the difference in the location of the bow shock in the forebody to be less than 10%.

1.9. Discussion

There are many similarities seen in the NS and DSMC wake flow computations for HEG Run 132 and LENS Case E. However, there are also many significant differences. It has been noted that the current DSMC work appears to have insufficient resolution and statistical representation of the flow in the near wake immediately behind the blunt body near the sting. However, we have no good indicators so far as to the quality of the NS computations, outside of their convergence criterion and the mesh-insensitivity of the results. An examination of the DSMA results using the Bird breakdown parameter can shed some light on the accuracy of the NS code in this application.

The Bird breakdown parameter, P, is defined as[39]

$$P = \frac{u}{\rho v}\left|\frac{d\rho}{ds}\right| = \frac{\lambda u}{\rho v_s}\left|\frac{d\rho}{ds}\right|$$

where u = velocity

• = density

• = collision frequency

s = distance along a streamline

• = mean free path

v_s = average molecular speed

In Bird's analysis, the onset of rarefaction effects was seen at 0.02, which is similar to the usual critical Knudsen number (mean free path divided by a characteristic length) of 0.01. In a recent study by Gilmore and Gallis[40], an entropy formulation of the onset of continuum breakdown in expanding flows indicated an even earlier onset than would be indicated by the parameter P. Fig. 17 shows a calculation of the P from the HEG Run 142 DSMC results. It is seen that near the shoulder of the body, P is in excess of 0.05. Even if the DSMC results have less than the desired statistical accuracy in the corner where the body and sting mate, one can conclude from this plot that near the separation point on the shoulder, the NS computation is being pushed beyond its limits. In this region, the DSMC has sufficient resolution and numbers of particles.

Even under conditions where the NS code may be exhibiting breakdown, there are strong similarities seen in some aspects of the NS and DSMC code computations (density, Mach contours particle paths, etc.). However, caution must be exercised in interpreting NS code results for these test conditions and those at lower densities, such as LENS Cases B and C. in addition of a slip boundary condition on the body might enable the NS codes to more accurately represent flow fields such as these and the other test cases that have been studied. Also, continued DSMC modeling efforts using finer grids in the near wake regions, and more particles overall will prove beneficial. This will surely require massively parallel computing machines or significant advances in computing architectures to achieve results quickly.

1.10. Conclusions

Improvements have been made in the NEQ2D code that have produced mesh-independent Navier-Stokes computational results for a 70-degree blunt cone model. The results for the

forebody region were significantly different from previous efforts by Stewart and Chen, who used an older version of the code. Both aforementioned forebody computations show a reasonable agreement with each other, but the current work shows a significant improvement in matching the shape of the normalized heat flux. However, there is a 23% difference in the stagnation point heat flux for the present work, in comparison with NASA Ames 41-inch shock tunnel data. Also the new results underpredict the forebody heat flux, which was the reverse of the previous work.

The Navier-Stokes code NEQ2D was also used to make comparisons with experimental data from the LENS and HEG shock tunnels for the sting-mounted AGARD 70-degree blunt cone model. Normalized computational heat fluxes showed reasonable agreement with the experimental data in the forebody. However, the dimensional computed heat flux values in the forebody showed a 37% difference at the stagnation point, compared to data from the HEG facility. Results for the LENS forebody heat flux data showed the same type of underprediction as in the case of the NASA Ames data. The Navier-Stokes code was also used to generate a computational interferogram for comparison to experimental results from HEG Run 133. The agreement for this comparison was excellent, and the location of the bow shock differed less than 10% with experiments.

Navier-Stokes computations were also presented for the wake region along the sting and compared to data form HEG and LENS. Here, the two sets of experimental heat flux data differed dramatically. The location of the computed heat flux maximum on the sting compared well with the HEG data, but he magnitude was underpredicted by almost a factor of 4. The reverse was the case for the LENS data, where the magnitude of the computed heat flux matched the LENS data, but the experimental heat flux maximum was located further down the sting. One possible explanation for this difference could be the existence of a turbulent shear layer in the wake. The turbulent shear layer would increase the surface heat transfer due to increased mixing and would also affect the turning angle of the wake flow and the shear layer impingement point on the sting (location of local heating maximum).

The DSMC and Navier-Stokes computations showed many areas of agreement with each other, as well as areas where they differed significantly. Density and Mach number contours show reasonable global agreement with supersonic regions immediately behind the blunt body. Additionally, both codes predicted the main recirculation zone, but the Navier-Stokes codes showed two smaller recirculation zones, which did not appear in the HEG Run 132 case. However, traces of the small recirculation zone near the shoulder of the body did appear in the LENS Case E DSMC results. Thermal non-equilibrium was indicated by both codes along the sting near the blunt body, but the normalized vibrational temperatures differed significantly over most of the flow-field. The DSMC code exhibited a difficulty in accurately computing the flow in the corner where the sting meets the rear of the blunt body. The difficulty is due to insufficient grid resolution, and too few particles in cells for that region.

The DSMC heat flux result showed almost an opposite behavior in comparison to the Navier-Stokes computations. The magnitude of the DSMC heat fluxes for the HEG Run 132 case was only 18% below the experimental data. However, the DSMC heat flux for LENS Case E

was overpredicted by a factor of 2.8. Also, the location of the peak heating along the sting moved farther from the body compared to the Navier-Stokes results, showing a better correlation to the peak heating in the LENS Case E data. Both of these results are opposite from the Navier-stokes computational results.

The DSMC results also indicated that the degree of rarefaction is high enough in portions of the near-wake region, especially at the shoulder, near the separation point. The Bird breakdown parameter exceeds 0.6 at that point, well in excess of any commonly used indicator of breakdown in Navier-Stokes computations. Hence, care must be exercised in the interpretation of any Navier-Stokes code results for this application. Further work using slip boundary conditions for the Navier-Stokes code and more refined grids for the DSMA codes may give improved results. For the DSMC work, this will probably require massively parallel machines in order to achieve results in a reasonable amount of time.

Unsteadiness is another issue, which could affect the interpretation of the flow-field data and computations. There is some ambiguity in the analysis of the shock tunnel data, which makes it unclear whether the impulse facility flow has been established or not. Additionally, there is computational evidence to show that the three-dimensional wake flow ins inherently unsteady. Issues of three-dimensionality, turbulence, and unsteadiness will all have to be addressed, both computationally and experimentally, before a complete understanding of the blunt body flow-field in impulse shock tunnel facilities is possible.

4. PROGRESS IN OTHER REAL-GAS AREAS

In addition to the major blunt cone activities, a number of related topics have been pursued in the real gas aerodynamic community. As closest to the blunt cone blunt side activity the work by Wen en Hornung[42] on the shock standoff distance off a sphere should be reported.

Wen and Hornung analyzed the standoff distance in terms of two similarity parameters, the free stream energy parameter

$$\mu = \frac{U_\infty^2 M}{\Theta_d \Re} \quad \text{and}$$

the reaction rate parameter

$$\Omega = \left(\frac{d\alpha}{dt}\right)_{sh} \frac{R_{Body}}{U_\infty}$$

Here U_∞ is the uniform free stream velocity, Θ_d the characteristic temperature for dissociation of a diatonic gas, $\Re$ the universal gas constant, M the molecular weight of the gas, α the mass fraction of the atomic component of the gas and R_{Body} the radius of the sphere. The index sh refers to the value directly behind the shock wave.

The free steam energy parameter μ determines whether the dissociation reaction in the flow has to be accounted for, and is essentially the same as the one used to characterize the HEG in its form h_0/h_{N2} in many references about the HEG, e.g.[18,25].

The reaction rate parameter, Ω, is a measure of the deviation from equilibrium of the gas behind the shock. $\Omega \rightarrow 0$ represents the frozen limit, $\Omega \rightarrow \infty$ the equilibrium limit. Between these limits the gas between the shock and the blunt body is in chemical non-equilibrium.

A significant effect that results from chemical reactions in the flow is the change of gas density behind the bow shock wave. The shock wave standoff distance is inversely proportional to the average density on the stagnation streamline in the shock layer. While in the case of a non-reacting flow and an infinitely fast reacting flow the density along the stagnation streamline stays

approximately constant, for non-equilibrium flows this is not the case.

Figure 18, which has been taken from Wen and Hornung[42] shows a typical calculated plot for density profiles in the shock layer along stagnation streamlines for different values of the reaction rate parameter Ω. The free-stream condition, and hence μ, was kept constant here, while the body radius and hence Ω was varied. Also, the influence of the boundary layer was neglected here. It can be seen that for the non-equilibrium case the density increases from the frozen value directly at the shock wave approximately linearly until it reaches the value at the body or the equilibrium value. In the above work this approximation was used to develop an analytical method which predicts the dimensionless shock wave standoff distance as a function of a reaction rate parameter. The result of the application of this analysis is shown in Fig. 19 for free-stream condition 1 in HEG in pure nitrogen, where the reaction rate parameter can be easily calculated and the blunt model used was a cylinder rather than a sphere. Although it has been shown that the analysis of the shock layer confirms that non-equilibrium effects are produced in the free piston driven shock tunnels, quantitative discrepancies between experiment and calculations remain just like in the blunt cone activities[43].

5. SUMMARY

The objective of the real-gas element of the WG18 activity was to identify the status of our simulation capability of the hypervelocity flight environment of aerospace vehicles. Such capability will be necessary for the design optimization of future aerospace transportation systems for access to space and space exploration where the requirements of reliability, reusability, performance, and cost are important considerations. Such missions will include, but are not limited to, future manned missions to Mars and a permanent presence of man in cis-lunar space. Additional applications will be found in unmanned applications where improved performance and cost benefits are important, such a repeated transportation of material in cis-lunar space or the transportation of large mass in the near solar system.

An attempt to identify current capability and shortcomings has been made, and an approach to address the shortcomings has been proposed. Specifically, current ground test simulation capability for hypervelocity flight in air has been described, and the corresponding capability of real-gas CFD simulation has been illustrated.

In our real-gas ground test facilities, there is a critical need to accurately describe the flow quality and to calibrate the facility in regards to reacting flow phenomena. Such a need is clearly manifested when one attempts to compare test results from one facility with another or when test results from a facility are used to verify, or to develop, CFD simulation tools. A critical element of the solution to this shortcoming is the development and application of state-of-the-art instrumentation and diagnostics.

Of course there are several limitations in our capability to simulate flight conditions with our current ground test facilities, particularly regarding physical scale, test time, and reproduction of actual flight environment, but these issues are discussed in another section of this report.

In the area of real-gas CFD all of the accomplishments and shortcomings of the perfect gas capability are apparent, including success and the lack thereof in the areas of turbulence and

transition and grid structure and resolution. Additional capability associated with real-gas phenomena indicates success in modeling reacting air in a compressive flow environment but shows less success where the flow is expanding and rarefaction, freezing, and non-equilibrium three-body atomic collision effects are important. Additionally, difficulties modeling turbulence and transition are compounded, and treatment of boundary conditions can require special attention. Also, unsteady phenomena in a real-gas environment are not adequately treated due to limitations in computing resources.

The recommended approach to developing an adequate simulation capability for hypervelocity flight is identified in the following critical steps:

1. Continue development of state-of-the-art instrumentation and diagnostics for high enthalpy real-gas flows in our ground facilities. Emphasis should be on non-intrusive optical diagnostics capable of accessing thermodynamic state of the gas and of providing quantitative data and qualitative imaging necessary in the description and understanding of the flow and for developing and verifying CFD models and tools.

2. Synergistic application and development of real-gas ground test and real-gas CFD is imperative! The CFD must be used in the definition of ground test experiments and in the interpretation of test results. Conversely, the ground test data must be used to verify the CFD models and simulation results. CFD simulations must include simulation of the flow environment produced in the ground test facility.

3. The approach illustrated with the WG18 blunt cone activity, in which a common model is tested in a variety of real-gas facilities, with common instrumentation, is recommended whenever possible.

4. Maintain a steady development of CFD tools with emphasis on reacting flow model enhancement and verification for non-equilibrium conditions, particularly for expanding flows, and emphasis on improvement in numerical issues involving discretization errors and boundary condition. Issues with turbulence modeling and transition in high enthalpy compressible flows are not easily tractable and demand a sustained and focused program over the long term.

5. To finalize the development of simulation capability verification with flight data will be ultimately required. This requirement should be considered in developing ground test campaigns and in developing and applying CFD methods.

6. ACKNOWLEDGEMENTS

The contributions of Drs. L. Gochberg and G. Allen[41] comprise a large part of this work and are gratefully acknowledged.

7. REFERENCES

1 "Hypersonic Experimental and Computational Capability, Improvement and Validation", edited by Saric, W.S., Muylaert, J., and Dujarric, C., AGARD-AR-319 Vol. 1, May 1996.

2 Moss, J.N., Mitcheltree, R.A., Dogra, V.K., and Wilmouth, R.G., "Direct Simulation Monte Carlo and Navier-Stokes Simulations of Blunt Body Wake Flows", AIAA Journal, 32 (7) 1399-1406 (1994).

3 Allègre, J., and Bisch, D. "Experimental Study of a Blunted Cone at Rarefied Hyper-

sonic Conditions", Laboratoire D'Aerothermique RC 94-7, Centre National de la Recherche Scientifique (1994).

4 Gallis, M.A. and Harvey, J.K., "Comparison of the Maximum Entropy DSMC Code with Flowfield Measurements", AIAA Paper 95-0413 (1995).

5 Legge, H., "Heat Transfer and Forces on a Blunted 70 Degree Half Angle Cone Measured in Hypersonic Free Jet Flow", IB 222-93 A33, Institut für Experimentelle Strömungsmechanik, DLR, Göttingen (1994).

6 Gilmore, M., "Test Case 6 – Rarefied Flow Over a Blunt Body", 4th European High Velocity Database Workshop ESTEC, Noordwijk, The Netherlands (1994).

7 Pallegoix, J.-F., "Workshop ESTEC – Test Case No. 6 – Rarefied Spherically Blunted Cone", 4th European High Velocity Database Workshop ESTEC, Noordwijk, The Netherlands (1994).

8 Hash, D.B., Hassan, H.A., Dogra, V.K., and Price, J.M, "Navier-Stokes Calculations for a Spherically Blunted Cone (LENS Condition)", 4th European High Velocity Database Workshop ESTEC, Noordwijk, The Netherlands (1994).

9 Kastell, D., Horvath, T.J., and Eitelberg, G., "Non-equilibrium Flow Expansion Experiment Around a Blunted Cone", 4th European High Velocity Database Workshop ESTEC, Noordwijk, The Netherlands (1994).

10 Holden, M., Kolly, J., and Chadwick, K., "Calibration Validation and Evaluation Studies in the LENS Facility", 33rd Aerospace Sciences Meeting, AIAA Paper 95-0291 (1995).

11 Candler, G.V. and MacCormack, R.W., "Computation of Weakly Ionized Hypersonic Flows in Thermochemical Non-equilibrium", Journal of Thermophysics and Heat Transfer, 5 (3) 226-273 (1991).

12 Stewart, D.A., and Chen, Y.K., "Hypersonic Convection Heat Transfer over 140 Degree Blunt Cones in Different Gases", Journal of Spacecraft and Rockets, 31 (5) 735-743 (1994).

13 Park, C., "Assessment of Two-temperature Kinetic Model for Ionizing Air", Journal of Thermophysics and Heat Transfer, 3 (3) 233-244 (1989).

14 Chan, W.M., Chiu, I.-T., and Buning, P.G., "User's Manual for the HYPGEN Hyperbolic Grid Generator and the HGUI Graphical User Interface", NASA TM 108791 (October, 1993).

15 Koura, K., and Matsumoto, H., "Variable Soft Sphere Molecular Model for Air Species", Physics of Fluids A, 4 (5) 1083-1085 (1991).

16 Leving, R.D., and Bernstein, R.B., "Molecular Reaction Dynamics and Chemical Reactivity", Oxford University Press (1987).

17 Loubsky, W.J., Hiers, R.S., and Stewart, D.A., "Performance of a Combustion-Driven Shock Tunnel with Application to the Tailored-Interface Operating Conditions", Proceedings of the 3rd Conference on Performance of High Temperature Systems, Paper 30, p. 547-559 (1964).

18 Eitelberg, G., McIntyre, T.J., Beck, W.H., and Lacey, J., "The High Enthalpy Shock Tunnel in Göttingen", AIAA Paper 92-3942 (July, 1992).

19 Holden, M.S., "Large Energy National Shock Tunnel (LENS) Description and Capabilities", CALSPAN-UB Research Center, Buffalo, NY (February 1991).

20 McIntosh, M.K., "Computer Program for the Numerical Calculation of Frozen and Equilibrium Conditions in Shock Tunnels", Department of Physics, Australian National University, Canberra (December, 1968).

21 Lordi, J.A., Mates, R.E. and Moselle, J.R., "Computer Program for the Numerical Solution of Non-equilibrium Expansions of Reacting Gas Mixtures", NASA CR-472 (May, 1966).

22 Radhakrishnan, K., and Bittker, A.D., "LSENS, A General Chemical Kinetics and Sensitivity Analysis Code for Gas-Phase Reactions: User's Guide", NASA TM-105851 (January, 1993).

23 Vardavas, I.M., "Modelling Reactive Gas Flows Within Shock Tunnels", Australian Journal of Physics, 37 (2) 157-177 (1984).

24 Hannemann, K., and Brenner, G., "Numerical Simulation of Reacting Flows Related to the HEG", Proceedings of the 19th International Symposium on Shock Waves, Marseilles (July, 1995).

25 Eitelberg, G., "First Results of Calibration and Use of the HEG", AIAA Paper 94-2525 (June, 1994).

26 McGrory, W.D., Slack, D.C., Applebaum, M.P., and Walters, R.W., "The General Aerodynamic Simulation Program", GASP Version 2.2, User's Manual, Aerosoft Inc. (1993).

27 Papadopoulos, P., Tokarcik-Polsky, S., Venkatapathy, E., and Deiwert, G.S., "The NASA Ames 16-Inch Shock Tunnel Nozzle Simulations and Experimental Comparison", AIAA Paper 95-6038, 6th International AIAA Aerospace Plane and Hypersonic Technologies Conference (April, 1995).

28 Kastell, D., private communication (1995).

29 Heirs, R.S. Jr., and Reller, J.O. Jr., "Analysis of Non-equilibrium Air Conditions in the Ames 1-Foot Shock Tunnel", NASA TN-D 4985 (1969).

30 Candler, G.V., private communication (1995).

31 Chen, Y.K., private communication (1995).

32 Horvath, T.J., private communication (1995).

33 Kidd, C.T., Nelson, C.G., and Scott, W.T., "Extraneous Thermocouple EMF Effects Resulting From the Press-Fit Installation of Coaxial Thermocouples in Metal Models", Proceedings of the ISA 40th International Instrumentation Symposium, Paper No. 94-1022, p. 317-335 (1994).

34 Legge, H., "Experiments on a 70 Degree Blunted Cone in Rarefied Hypersonic Wind Tunnel Flow", AIAA Paper 95-2140 (June, 1995).

35 Anagnost, A.J., "Time Accurate Simulation of Hypervelocity Base Flows on Massively Parallel Computers", Ph. D. Dissertation, Department of Aeronautics and Astronautics, Stanford University, SUDAAR 653 (1994).

36 Haas, B.L., "Mars Pathfinder Computations Including Base-Heating Prediction", AIAA Paper 95-2086 (June, 1995).

37 Holden, M.S., Chadwick, K.M., Gallis, M.A., and Harvey, J.K., "Comparison Between Shock Tunnel Measurements on a Planetary Probe Configuration and DSMC Predictions", Proceedings of the 20th International Symposium on Shock Waves, Pasadena (July 1993).

38 Yates, L.A., "Images Constructed From Computed Flowfields", AIAA Journal, 31 (10) 1877-1884 (1993).

39 Bird, G.A., Molecular Gas Dynamics and the Direct Simulation of Gas Flows", Clarendon Press, Oxford (1994).

40 Gilmore, M.R. and Gallis, M.A., "Breakdown of Continuum Solvers in Rapidly Expanding Flows", AIAA Paper 95-2134 (June 1995).

41 Gochberg, L.A., Allen, G.A. Jr., Gallis, M.A., and Deiwert, G.S., "Comparison of Computations and Experiments for Non-equilibrium Flow Expansions Around a Blunted Cone", AIAA Paper 96-0231 (January 1996).

42 Wen, C.-H., and Hornung, H., "Non-equilibrium Dissociating Flow Over Spheres", J Fluid Mech 199; 389-405 (1995).

43 Kastell, D., Carl, M., and Eitelberg, G. "Phase Step Holographic Interferometry Applied to Hyperveloity, Non-equilibrium Cylinder Flow", Experiments in Fluids 22; 67-66 (1996).

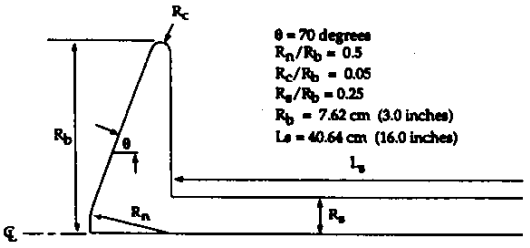

Fig. 1 Geometry for the 70° blunt cone test model

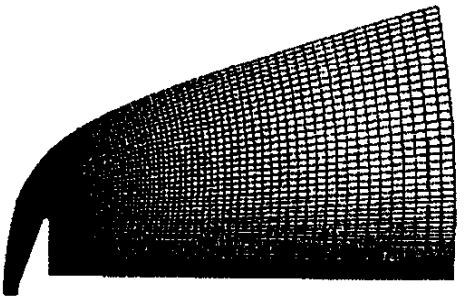

Fig. 2a Mesh from NS code simulation of blunt body flow

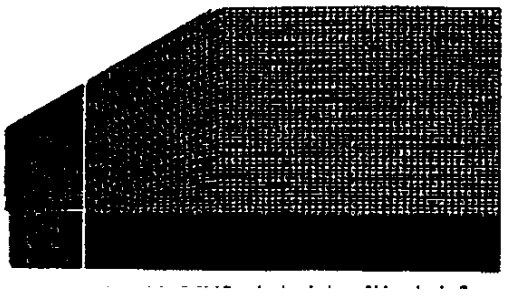

Fig. 2b Mesh used for DSMC code simulation of blunt body flow

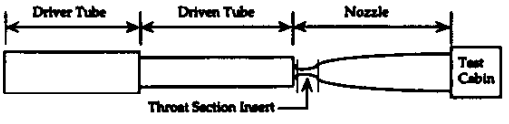

Fig. 3 Schematic of a generic shock tunnel facility (not to scale)

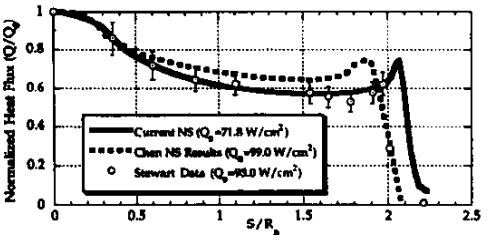

Fig. 4 Normalized forebody heat fluxes from NS computations, and Chen and Stewart data and computations

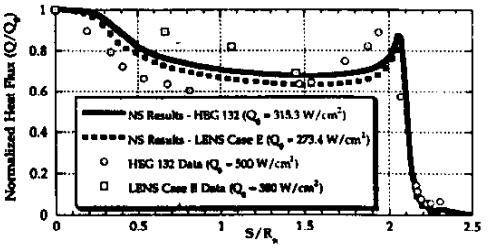

Fig. 5 Normalized forebody heat fluxes from NS computations, HEG run 132 data, and LENS case E data

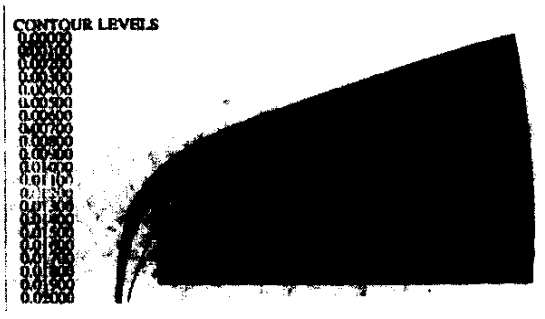

Fig. 6 HEG run 132 density contours from NS computations

Fig. 7 HEG run 132 particle paths from NS computations

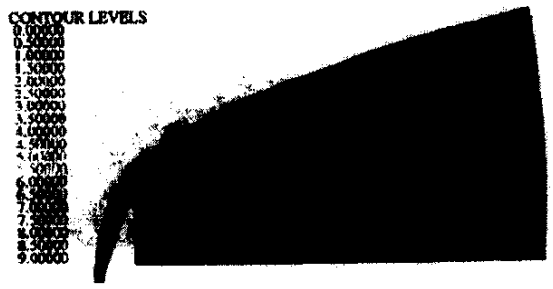

Fig. 8 HEG run 132 Mach number contours from NS computations

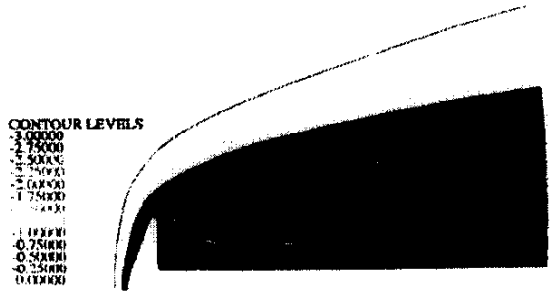

Fig. 9 HEG run 132 normalized vibrational temperature from NS computations

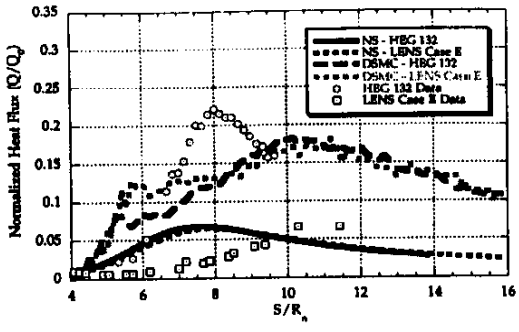

Fig. 10 Normalized heat fluxes from wake flow NS and DSMC computations compared to experimental data

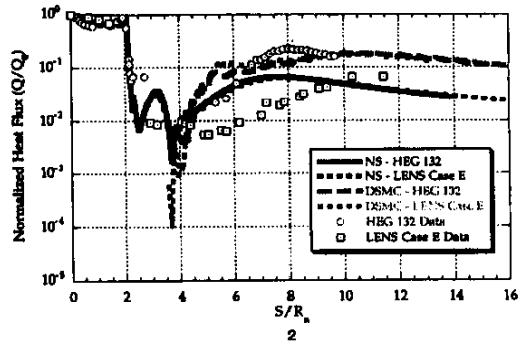

Fig. 11 Normalized heat fluxes from NS and DSMC computations compared to experimental data for entire flow field

Fig. 12 HEG run 132 density contours from DSMC computations

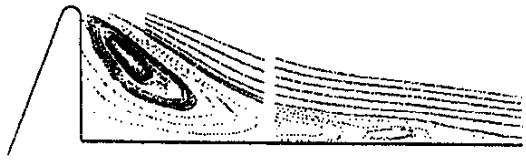

Fig. 13 HEG run 132 particle paths from DSMC computations

Fig. 14 HEG run 132 Mach number contours from DSMC computations

Fig. 15 HEG run 132 normalized vibrational temperature from DSMC computations

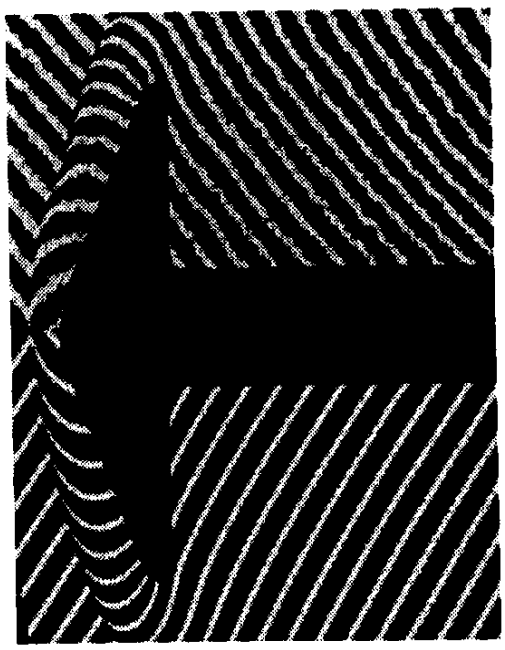

Fig. 16 Experimental and computational interferograms from HEG run 132

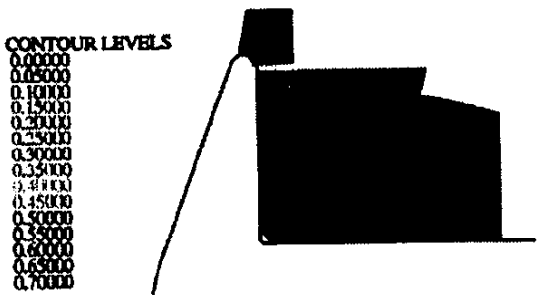

Fig. 17 Bird breakdown parameter from HEG run 132 DSMC computations

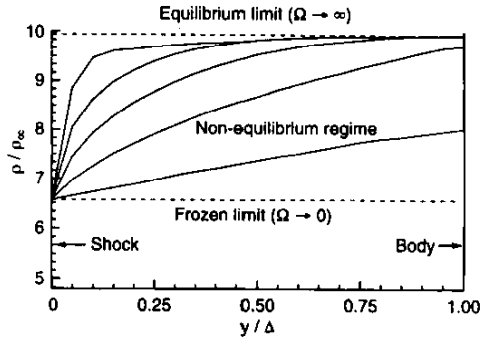

Fig. 18 Pilot of density profiles on stagnation streamlines of spheres for equilibrium, frozen and non-equilibrium flows. The five intermediate density profiles represent flow over spheres of five different radii of 0.025, 0.25, 1, 3 and 60 inch with the same free stream conditions (U_∞ = 5.2 m/s, ρ_∞ = 0.043 kg/m^3, T_∞- 2300 K and α_∞ = 0.0156) (Wen and Hornung)[42]

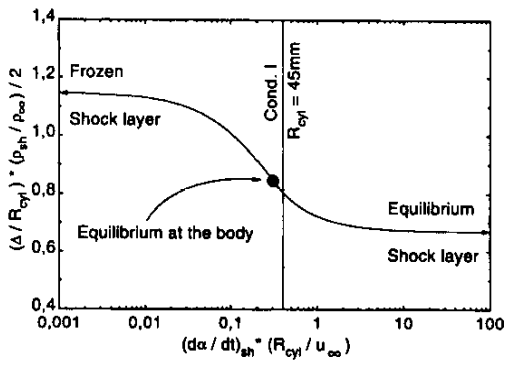

Fig. 19 Dimensionless shock wave standoff distance over reaction rate parameter obtain using Wen and Hornung's analytical method for pure nitrogen at HEG condition 1